Suitability of remote sensing for dust storm detection and quantification in Sahelian Africa

Wimala van Iersel

Universiteit Utrecht

Suitability of remote sensing for dust storm detection and quantification in Sahelian Africa

MSc Thesis

March 2014

Author: Wimala van Iersel

Student number: 3717968

E-mail: w.k.vaniersel@students.uu.nl

First supervisor: Geert Sterk

Second supervisors: Steven de Jong

and Maarten Zeylmans van Emmichoven

MSc Programme: Earth Surface and Water

Faculty of Geosciences

Department of Physical Geography

Utrecht University

Abstract

Wind erosion is one of the main soil degradation processes that play a role in desertification in Sahelian Africa. Development in remote sensing techniques during the last decade has increased its potential for desertification assessment. The purpose of this study was to develop an empirical method to quantify wind erosion with satellite imagery for dryland areas in Sahelian Africa. Firstly, dust storms in the Sahel region were identified on the available InfraRed Imager of the Meteosat Second Generation instrument (SEVIRI-MSG) images in 2013. Additionally, the storms had to be recorded by at least one Aerosol Robotic Network (AERONET) observation station in the Sahel. Secondly, the relation between Aerosol Optical Thickness (AOT) and dust concentration at ground level was determined. Since dust concentration measurements were only available for 2006, AOT was used a proxy for dust concentration. Thirdly, the statistical relation between brightness temperature (BT) and AOT measured in-situ was determined and eventually the relation between BT and dust concentration was obtained. Finally, the empirical method was applied on two SEVIRI-MSG images. Two linear regression equations were developed to describe dust concentration in months February-March of the dry season at two measurement stations in the Sahel. Poor relations were found for the early rainy season months. Application of the obtained equations on two SEVIRI-MSG images revealed unrealistic dust concentrations, which could not be validated with currently available ground data. Another important conclusion was that the dust storms causing most wind erosion problems, which occur in the early rainy season, are often not detectable on the SEVIRI-MSG images because their signal is blocked by the cloud of the thunderstorms above it. Therefore, quantification of annual wind erosion with the obtained equations without inclusion of these events will lead to significant underestimation of sediment transport.

Table of contents

1. Introduction

1.1 Desertification in Africa

The importance of land degradation among global issues is enhanced because of its impact on world food security and quality of the environment (Eswaran et al., 2001). In a general sense, land degradation in the Earth's drylands is referred to with the term "desertification". Drylands can be defined based on the aridity index, which is defined as the average annual precipitation divided by the potential evapotranspiration (UNEP, 1997). Drylands have an aridity index of 0.05-0.65 (UNCCD, 2011), thus excluding hyper arid regions like the Sahara. In the process of desertification, dryland areas become significantly less biologically productive (WMO, 2010). Desertification is experienced on 33% of the global land surface and affects more than one billion people, half of whom live in Africa (Eswaran et al., 2001). Dregne and Chou (1992) estimated that 73% of the land surface in Africa is degraded due to desertification processes. Agricultural yield reduction in Africa due to past soil erosion may range from 2 to 40%, with a mean loss of 8.2% for the continent (Eswaran et al., 2001). Moreover, Africa is sensitive to climate change, because of its extreme climates (Jones et al., 2013). Africa also has less resilience to cope with these changes due to its developing status and low financial resources (UNCCD, 2011).

1.2 Large scale assessments

An accurate estimation of the area of desertified land and quantification of the occurring desertification in Africa is still lacking. This is due to the complexity of the desertification phenomenon: its multi-disciplinary causes, which are often interacting with each other (Geist, 2005). Up till now, actual area of desertified land has at best been investigated qualitatively in 1992 with The Global Assessment of Soil Degradation (GLASOD), which assembled the expert judgments of many soil scientists to produce a world map of human-induced soil degradation. The GLASOD has been much criticized, but it is by far the best representation of global soil degradation available up to now (WMO, 2010).

Satellite remote sensing has been used extensively in attempts to monitor desertification (WMO, 2010). During the Global Assessment of Land Degradation and Improvement (GLADA) remotely-sensed normalized difference vegetation index (NDVI) has been used as a proxy for net primary production (NPP), which is expected to decrease during the process of desertification (Bai et al., 2008). However, the GLADA results have been criticised for its methodological problems (Wessels, 2009; Vogt, 2011). For example, the regression performed between NDVI and NPP was based on a large number of pixels across the globe at a single moment in time. Therefore, it does not test the ability of NDVI to predict NPP on over time on annual basis, instead it merely shows a strong relationship between NDVI and NPP across the globe.

To get more insight in the process of desertification and its status in Africa, it will be essential to explore methods to quantify it on a continental scale. Satellite remote sensing data may be useful for this purpose: it may give quantitative information for model parameters to simulate desertification and erosion processes or it may even deliver direct information on loss of soil (Lantieri, 2006). From literature can be concluded that the main indicators of desertification are non-climate related vegetation degradation and increased occurrence of soil degradation processes (Symeonakis and Drake, 2004). Remote sensing can be useful for the measurement of these indicators, for example by determining the vegetation cover and monitoring large scale soil degradation features.

Development in remote sensing techniques during the last decade has increased its potential for desertification assessment (Lantieri, 2006). Temporal resolution up to 15 minutes provided by geostationary Spinning Enhanced Visible and InfraRed Imager of the Meteosat Second Generation instrument (SEVIRI-MSG) offers new opportunities to monitor highly dynamic features on the Earth's surface and in the atmosphere (EUMETSAT, 2004). One of the new possibilities is the detection of erosion processes creating features of kilometre scale, like dust storms as a form of wind erosion.

1.3 Wind erosion processes

Wind erosion is one of the main soil degradation processes that play a role in desertification (WMO, 2010). According to Oldeman (1994) wind erosion is the main soil degradation process in the African dryland areas, affecting 186 million ha. In drylands often the erosivity of the wind as an eroding agent is high, due to lack of a significant vegetation cover, and the erodibility of the soil is high, due to low organic matter content. Therefore, the African drylands are often prone to severe forms of wind erosion.

Jones et al. (2013) describe three types of wind erosion processes: suspension, saltation and surface creep. During suspension fine particles less than 0.1 mm in size are moved parallel to the surface then upward into the atmosphere by strong winds, returning to the ground only when the wind subsides or with precipitation. Even though suspended particles make up only a minority of the total movement of soil by wind, they can travel up to thousands of kilometres. In saltation particles bounce short distances along the surface, dislodging additional particles with each impact. The bouncing particles, ranging in sizes from 0.1 to 0.5 mm, usually remain within 30 cm of the surface. This process accounts for 50 to 90% of the total movement of soil by wind. Larger soil particles roll and slide along the ground surface during the process of surface creep, often aided by impacts of saltating particles.

Unfortunately, wind erosion does not leave many clear detectable landscape features like for example water erosion does with gullies. However, because of the threshold velocities needed to initiate particle movement most particle transport takes place

during short, intense dust storms (Sterk, 2003). These dust storms take place on a spatial scale of several kilometres. In addition, dust storms originating from the hyper-arid regions like the Sahara also form a source of dust particles for drylands if deposition takes place (WMO, 2010).

1.4 Large scale dust quantification with thermal infrared radiation

Research in the field of detecting dust storms with remote sensing has taken a large leap forward in recent years (Shao, 2008). This is among other things due to the role of the dust particles in aerosols, which are colloids of fine particles or droplets in air or another gas (Hinds, 1999). Aerosols are important in climate research because of their effect on radiation (Xu et al., 2011; Knippertz and Todd, 2012; Schepanski et al., 2012; Akhlaq et al., 2012). In order to obtain dust concentrations from satellite images Zhang et al. (2006) composed an algorithm to calculate dust column density from variables, which could be obtained from aerosol optical thickness (AOT), which is a proxy for dust loading (Marticorena et al., 2010), and particle effective radius retrieved from the satellite images. The algorithm was developed with Moderate Resolution Imaging Spectroradiometer (MODIS) images from the Gobi desert. The dust algorithm works with the specific properties of dust particles in 8.5 μm, 11 μm and 12 μm of the thermal infrared radiation (TIR). The so-called brightness temperature (BT) of these channels does not show typical behaviour, because of its substantial dependence on the surface temperature. However, the brightness temperature difference (BTD) between 11 and 8.5 μm and between 12 and 11 μm wavelengths can be used to correct for this background signal of the desert surface and to help discriminate between dust and other objects. However, they also mentioned that their results required validations with in situ measurements. Unfortunately, no information on validation of their results is available in literature.

Li et al. (2007) used the same algorithm by Zhang et al. (2006) to monitor and quantify a dust event over the Sahara. Because they used images of the SEVIRI-MSG their dust algorithm worked with the TIR bands at 8.7 μm, 10.8 μm and 12.0 μm, comparable to the 8.5 μm, 11 μm and 12 μm channels of MODIS. Li et al. (2007) used a similar radiation transfer model as Zhang et al. (2006) to simulate transfer of the specific TIR wavelengths through dust clouds and link these to images of the SEVIRI-MSG. They concluded from their case study that the evolution of a dust storm is well depicted quantitatively by SEVIRI-MSG. Its high temporal resolution and good spectral coverage from a geostationary perspective offer a unique observational capability. Again, no validation with in-situ measurements of dust concentrations was performed. It will be challenging to develop a method to compare satellite observed dust storms with ground data. Although they are scarce, in-situ measurements of AOT and dust concentration from the Sahel region are available. The Aerosol Robotic Network (AERONET) of sun-photometers offers a ground-based aerosol monitoring system, which is also present in

North Africa. In addition, dust concentration has been directly measured at the so-called "Sahelian Dust Transect" (SDT). This is a set of three stations deployed along the main transport pathway of Saharan and Sahelian dust towards the Atlantic Ocean (Marticorena et al., 2010).

Quantification of the remotely sensed dust storms could contribute to the assessment of soil and nutrient losses due to wind erosion in Africa. A method to obtain dust concentrations from satellite images would be to find an empirical relation between the radiation delivered by the images and dust concentrations measured in-situ.

1.5 Objectives

The general objective of this study was to develop an empirical method to quantify wind erosion with satellite imagery for dryland areas in Sahelian Africa on the basis of in-situ measurements. More specific objectives to achieve this were:

1. To identify dust storms in the Sahel region on the available MSG images in 2013, which are also recorded by at least one AERONET observation station in the Sahel.
2. To determine the relation between aerosol optical thickness and dust concentration, both measured at observation stations at ground level.
3. To explore the relation between TIR measured at the top of the atmosphere and aerosol optical thickness measured in-situ and eventually dust concentration.
4. To develop an empirical method from the above-mentioned relations to derive lateral dust concentrations from the SEVIRI-MSG imagery.

2. Materials and Methods

2.1 Study area

In the Sahel (Figure 1), soils are sandy often with poor fertility, lacking phosphorus, nitrogen and humus, and have low water retention capacities (Koala and Bielders, 1997). These characteristics make soils susceptible to wind erosion. Wind erosion can become a problem whenever the soil is loose, dry, bare, or nearly bare, and the wind velocity exceeds the threshold velocity for initiation of soil particle movement (Sterk & Goossens, 2007). In the Sahel, winds that exceed the threshold wind velocity for soil particle movement may occur during two distinct seasons (Sterk, 2003). During the dry season (October-April) the area is subject to strong trade winds, called the Harmattan. These winds can cause dust storms of country or even continental scale and may reach high altitudes up to 5 km (Shao, 2008).

The most important wind erosion period in the Sahel is during the early rainy season (May-July) (Sterk, 2003), when the Inter-Tropical Convergence Zone (ITCZ) moves northward compared to its winter position. South-westerly monsoon winds bring warm, moist air, leading to an unstable atmosphere and formation of thunderstorms (Shao, 2008). They may even occur as groups called squall lines consisting of a longitudinal extension of approximately 300-500 km (Tetzlaff and Peters, 1986). The internal flow within the thunderstorms can lead to the formation of dust storms at the land surface with a longitudinal extension of approximately 5 km and much larger in the case of a squall line. The dust storms are usually of short duration, from a few minutes to one hour, but may result in high transport rates of soil particles (Sterk, 2003; Shao 2008). They can reach altitudes of several 100 m (Tetzlaff and Peters, 1986).

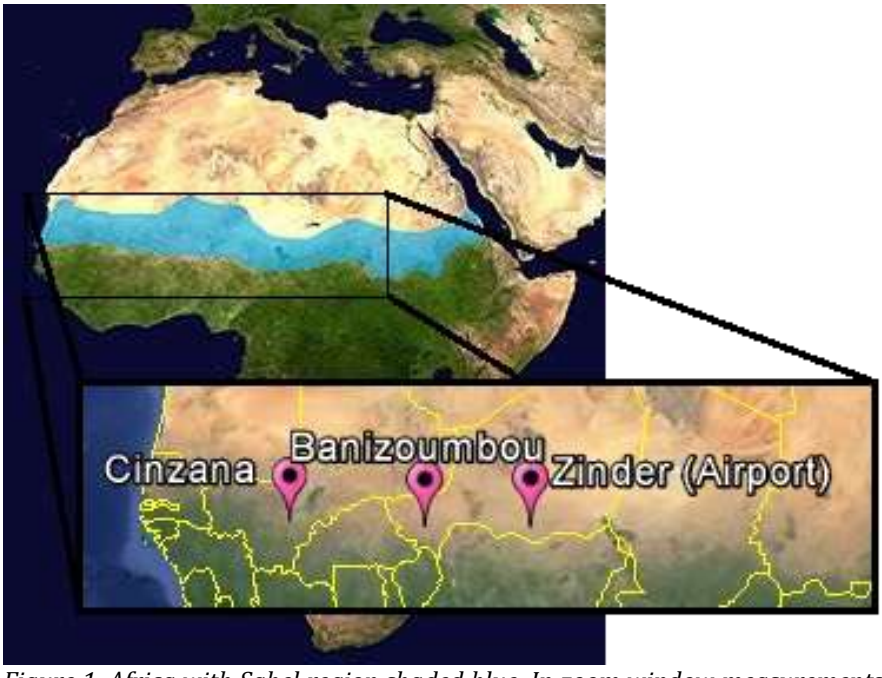

Figure 1. Africa with Sahel region shaded blue. In zoom window measurements stations Cinzana (Mali), Banizoumbou (Niger) and Zinder Airport (Niger).

Ground data used for this study was collected at the measurements stations in Cinzana (13°16'40" N, 05°56'02" W), Banizoumbou (13°32'27" N, 02°39'54" E) and Zinder Airport (13°46'37" N, 08°59'24" E) (figure 1).

2.2 Ground data

In order to attain an empirical method to quantify wind erosion by dust storms, a data set of TIR satellite imagery with brightness temperatures of the dust storms and databases with ground data of these storms were necessary. For the current study only images from 2013 were available. Daily mean dust concentrations from the SDT are online accessible for 2006-2008 via the online data base of the African Monsoon and Multidisciplinary Analysis (AMMA) project (AMMA, 2013a). Daily mean and point measurements of AOT are available online at the AERONET website from 2001 up to today for three stations in the Sahel (Figure 1) (AERONET, 2013). Since the imagery data and ground data are from different time periods with no overlaps, but AOT data is available for 2000-2013, AOT was used as a proxy for both dust concentration and brightness temperature from the images.

2.2.1 Dust concentration

AMMA is an international project to improve knowledge and understanding of the West African Monsoon and its variability (AMMA, 2013b). The AMMA project includes in-situ measurements of dust concentrations at locations in West Africa and in the Gulf of Guinea. They provide online accesses to their data base for the research community (AMMA, 2013b). It includes a data set called AE.Dust_ST, consisting of daily PM10 dust ($d<10$ µm) concentration measurements performed with the Tapering Element Oscillating Microbalance (TEOM) 1400a method (Manticorena et al., 2010). More precisely, PM10 means particulate matter which passes through a size-selective inlet with a 50% efficiency cut-off at 10 µm aerodynamic diameter. Measurements from two stations in West-Africa were used: Cinzana (13°16'48" N, 05°55'48" W) and Banizoumbou (13°32'24" N, 02°39'36" E) (Figure 1). Dust concentration is expressed as the daily mean concentration (µg m^{-3}). Data is accessible for the period 2006-2008, with exact dates differing between the stations. For this study the data for 2006 was used. In addition, sub-daily scale (5 min) PM10 measurements for 2006 were made available upon request by the Laboratoire Interuniversitaire des Systèmes Atmosphérique (LISA) for the stations Cinzana and Banizoumbou (Figure 1).

2.2.2 Aerosol optical thickness

The AErosol Robotic NETwork (AERONET) program is a federation of ground-based remote sensing aerosol networks established by NASA and PHOTONS (AERONET, 2013). However, it does not provide dust concentrations directly. Aerosol Optical Thickness (AOT) is the degree to which aerosols prevent the transmission of light by absorption or scattering of light. The AOT is defined as the integrated extinction coefficient over a vertical column of unit cross section, where extinction refers to the intensity of light (AERONET, 2013). AOT is calculated as the negative logarithm of the fraction of radiation that is not scattered or absorbed on a path, and is therefore a dimensionless

quantity. High AOT indicates a large quantity of aerosols, and thus a significant amount of absorption and scattering of radiation. Low AOT indicates clearer air with fewer aerosols and increased transmission of radiation.

AOT measurements are performed at four different wavelengths: 440 nm, 670 nm, 870 nm, and 1020 nm (Holben et al., 2001). This study used the AOT measured at a wavelength of 440 nm, because according to Rajot et al. (2008) there is a good correlation between dust concentrations measured at the surface (PM10) and AOT at 440 nm. However, no quantified relation was given by Rajot et al. (2008).

Since aerosol particles may be all kinds of particles in the atmosphere, a certain AOT value can also be caused by other particles than mineral dust (Li et al., 2013). For example, fine carbonaceous particles are seasonally produced by biomass burning in the Sahel region (Rajot et al., 2008). The size distribution of aerosols can be estimated from AOT (-), typically from 440nm to 870nm. The first derivative of AOT with wavelength in logarithmic scale is known as the Angstrom parameter (α);

$$\alpha = -\frac{d \ln AOT}{d \ln \lambda} = \frac{\ln AOT_{\lambda_1} - \ln AOT_{\lambda_2}}{\ln \lambda_1 - \ln \lambda_2} \qquad (2.1)$$

where α is the Angstrom parameter (-) , AOT is the aerosol optical depth (-), and λ is the wavelength (nm). This parameter can be calculated from two or more wavelengths using a least squares fit. The occurrence of the carbonaceous particles could be estimated by the Angstrom Exponent between 440 and 870 nm ($\alpha_{440-870}$), which is relatively high for the carbonaceous particles due to their small size and relatively low ($\alpha_{440-870} < 0.4$) when the quartz grains dominate the aerosol mass (Holben et al., 2001). Values of $\alpha_{440-870} > 2.0$ indicate fine mode particles (e.g., smoke particles) dominate the aerosol mass (Eck, 1999).

Another disturbing factor can be water vapour in the atmosphere, because humidity increases the AOT due to more water uptake by the aerosols (Myhre et al., 2007). The determination of total column water vapor or precipitable water (cm) by AERONET uses three channels: 675nm, 870nm, and 940nm. For more details on the calculation of precipitable water from AOT measurements see Schmid et al. (2001). In order to check for the disturbing effect of water vapour in the atmosphere on the AOT_{440} measurements, the relation between precipitable water (cm) and AOT was investigated. Precipitable water was obtained from the AERONET database.

AOT time series are easily accessible for around 40 stations divided over Africa. In the Sahel the stations in Cinzana, Banizoumbou and Zinder Airport (figure 1) have AOT data from 2000-2013 (Holben et al., 1998). Measurements are performed with an automatic sun and sky scanning spectral radiometer at variable times of the day and are available as point data and as daily mean values (AERONET, 2013).

2.3 The imagery data set

2.3.1 Data source

The satellite images for this study were acquired by the geostationary Spinning Enhanced Visible and InfraRed Imager of the Meteosat Second Generation instrument (SEVIRI-MSG). The European Organisation for the Exploitation of Meteorological Satellites (EUMETSAT), which owns this system and other comparable instruments, is an intergovernmental organisation created through an international convention agreed by a current total of 26 European Member States. EUMETSAT operates a system of meteorological satellites monitoring the atmosphere, ocean and land surface, which deliver weather and climate-related satellite data, images and derived products (EUMETSAT, 2010). An extra advantage of the EUMETSAT data and products is that they are provided via environmental data providers like the so-called GEONETCast data network (EUMETSAT, 2007). GEONETCast comprises a global network of data dissemination systems that share environmental data and derived products to a world-wide user community in near real-time (Kraaijenbrink, 2012).

The potential of GEONETCast data in geo-related research, in combination with the inexpensiveness of a receiving unit led to the instalment of a GEONETCast receiver by the Utrecht University Faculty of Geosciences in 2011. The current study is performed at this faculty. Although the received data did not seem to be below expectations, there were issues that withhold a direct use of the data by geo-researchers at the faculty. Those are described and partly remedied by Kraaijenbrink (2012).

The GEONETCast data products currently received by Utrecht University originate from multiple satellites (Kraaijenbrink, 2012). However, determined by the currently active licenses, the data with the largest spectrum of products is broadcasted by EUMETSAT. It comprises raw and derived data that originates from the Meteosat Second Generation (MSG) (EUMETSAT, 2004). A list with some of the available products is presented by EUMETSAT (2013). Especially the MSG image data was of interest for this study, because of its high temporal resolution (15 minutes) in combination with its geostationary position, acceptable spatial resolution (3x3 km) in relation to the kilometre scale at which dust storms occur, and thermal infrared (TIR) bands to observe dust storms at night.

2.3.2 Pre-selection of images with EUMETSAT RGB Dust product

In order to select the correct time frame to detect a dust storm on the images a manual pre-selection process was performed with the EUMETSAT MSG Dust product (Benincasa, 2012). The EUMETSAT MSG Dust product is a RGB composite based upon infrared channels IR 8.7, IR 10.8 and IR 12.0 of the SEVIRI-MSG. It is designed to monitor the evolution of dust storms over deserts during both day and night. The RGB composite is produced using the following SEVIRI-MSG channels: $IR_{12.0}$-$IR_{10.8}$ (on red), $IR_{10.8}$-$IR_{8.7}$

(on green); and $IR_{10.8}$ (on blue). It is the relative low value of the $IR_{10.8}$-$IR_{8.7}$ of dust clouds compared to desert sand which results in a relative lack in green, thus leading to a magenta/pink colour for dust clouds. Dry land looks from pale blue during daytime to pale green during night-time. Thick, high-level clouds have red-brown tones and thin high-level clouds appear as nearly black. Emissions and subsequent transport of regional scale individual dust events can be detected by their magenta/pink colour and followed in the RGB composite pictures. This was used in the pre-selection process.

The brightness temperature difference (BTD) between 10.8 and 8.7 μm and between 12.0 and 10.8 μm wavelengths are used to correct for the background signal of the desert surface and to help discriminate between dust and other objects (Zhang et al., 2006; Li et al., 2007). The $BTD_{12.0\text{-}10.8}$ value is the optimal to discriminate dust from other objects like clouds. This is because the value of $BTD_{12.0\text{-}10.8}$ is positive for dust clouds and negative for water/ice clouds due to a different absorption of the two wavelengths. The $BTD_{10.8\text{-}8.7}$ is optimal to discriminate between the background signal of the desert because the emissivity in 8.7 μm of small quartz mineral particles (0–45 μm) in the desert dust is much larger than the emissivity of sand-sized quartz particles (125–500 μm) resulting in relatively small $BTD_{10.8–8.7}$ values for dust storms (Lensky and Rosenfeld, 2008). The RGB combination used in the MSG dust product exploits this difference in emissivity of dust and desert surfaces. Because emissivity is measured in TIR it uses the temperature difference between the hot desert surface and the cooler dust cloud during day time. During night time this difference in temperature, and therefore emissivity, becomes smaller and it becomes more difficult to discriminate the dust storms from the desert surface.

2.3.3 Retrieving MSG imagery

The MSG images are only a small part of the total information received. The MSG images are provided in .hrit file format, which is not readable by common imaging process software, like ERDAS Imagine and ENVI. Therefore, the files were first converted to ENVI raster files accompanied by an ASCII header file (.hdr). This file type was chosen because further analysis was done in ENVI. In this file type the latitude-longitude grid was put on the image correctly and in degrees. This is necessary to locate the ground data measurement stations at a later stage. To convert these unreadable .hrit files to the ENVI file type the user interface MSG Data Retriever (appendix I) provided by ILWIS (Lemmens et al., 2009) was used. The next step was to create images during the selected time frames with the MSG Data Retriever interface using the channels IR 8.7, IR 10.8 and IR 12.0 with an interval of 15 min. The details on how this was performed can be found in appendix I.

2.3.4 Retrieving the BT from images

The images retrieved from GEONETCast were processed and each channel expressed in brightness temperatures (K). The RGB band combinations described above could be produced with the ENVI software for the manually selected spatial and temporal subset. To obtain brightness temperatures during a dust storm, the pixel values of the bands $BTD_{12.0\text{-}10.8}$; $BTD_{10.8\text{-}8.7}$ and $BT_{10.8}$ of the pixel (3x3 km) where the ground measurement station is located were stored per time step (15 min) in an ASCII file. These values were compared with the AOT values of the same temporal subset of the considered ground station.

2.4 Relation between BT and dust concentration

2.4.1 BT as proxy for AOT

An empirical relationship between the BT measurements from space and in-situ dust concentrations was derived. The first step was to determine a relation for the in-situ measured AOT and the BT from the three channels, which were already calculated into the bands $BTD_{12.0\text{-}10.8}$; $BTD_{10.8\text{-}8.7}$ and the original $BT_{10.8}$. This was done by a multiple linear regression analysis, with AOT being the dependent variable and the three BT bands as independent variables.

In addition, a principal component analysis (PCA) was applied for a couple of dust storms to investigate which BT band is mainly responsible for the appearance of the dust storm in the band combination $BTD_{12.0\text{-}10.8}$ (on red), $BTD_{10.8\text{-}8.7}$ (on green) and $BT_{10.8}$ (on blue). This PCA was done in ENVI with the spatial subset of just the magenta coloured dust storm in the RGB image. Details on how the eigenvalues of the principal components and their eigenvectors could be obtained are given in appendix II.

2.4.2 AOT as proxy for dust concentration

As mentioned in section 2.2.2, no quantified relation between dust concentrations measured at the surface (PM10) and AOT_{440} was given by Rajot et al. (2008). Therefore, in this study the daily and sub-daily PM10 measurements were used with simultaneously measured AOT in a linear regression to determine such relation. The linear regression was done for seasonal and monthly scale, focussing on the seasons in which dust storms mainly occur in the Sahel (section 2.1).

2.4.3 Dust concentration from brightness temperature

Finally, the relation between brightness temperature and AOT and the relation between AOT and dust concentration were combined in an equation to calculate PM10 (μg m^{-3}) dust concentration directly from brightness temperature. This equation was applied on all pixels of a dust storm on 18-03-2013 and on 24-06-2013 to derive the mass of suspended dust per pixel. This was done with the Band Math function in ENVI. The range of calculated values, obtained from the statistics of the spatial subset of the dust storms, was compared with in-situ observed dust concentrations of dust storms in 2006.

3. Results

3.1 Detected dust storm events

Two dust storms in March and four storms in May matched the data sets of MSG images and ground based AOT (table 1). Events were not taken into account if no increased AOT (>1.0) was measured. The coordinates of the pixel (3x3 km) in which the measurement station was located is also given. Dust storms with simultaneous recording of increased AOT were detected at the Cinzana and Zinder Airport stations. The dust storms events had to be quantified with AOT measurements, because no in-situ dust concentrations were available for the period for which the dust storms were detected on MSG images.

An example of the RGB Dust image of the storm on 18-03-2013 at 12:00 is given in Figure 2. The six selected dust storms were used to obtain the brightness temperatures, as explained in section 2.3.4.

Table 1 Selected dust storms from EUMETSAT MSG Dust product by Benincasa (2012)

Date	Time	Station	Coordinates of station pixel (WSG-84)
18-03-2013	08:00-13:00	Zinder	13 47' 21.3" N, 8 58' 0.8" W
23-03-2013	08:00-16:00	Zinder	13 48' 9.19" N, 8 59' 15.95" W
08-05-2013	08:30-23:00	Zinder	13 47'56.82" N, 8 58' 47.15" W
09-05-2013	00:00-22:00	Zinder	13 47'56.82" N, 8 58' 47.15" W
24-05-2013	07:30-14:00	Cinzana	13 18' 31.62" N, 5 56' 35.56" E
31-05-2013	10:30-13:00	Cinzana	13 17' 24.43" N, 5 57' 1.91" E

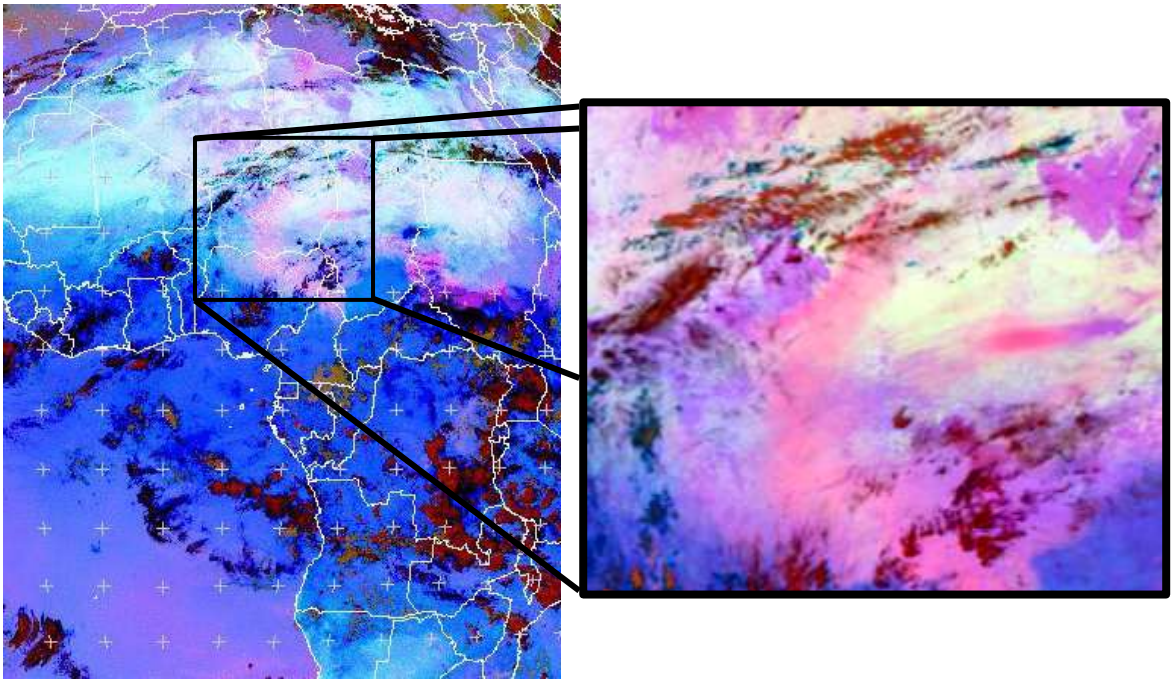

Figure 2 RGB Dust image of the 18-03-2013 event at 12:00. Overview image is taken from the EUMETSAT MSG Dust product by Benincasa (2012). Zoom window is the RGB composite in ENVI used for analysis. For both frames R: $IR_{12.0}$- $IR_{10.8}$, G: $IR_{10.8}$-$IR_{8.7}$, B: IR_{10}.

3.2 Relation between dust concentration and AOT (2006)

3.2.1 Disturbance of AOT due to carbonaceous particles and water vapour

As a first step, it was evaluated how the AOT values are disturbed by other factors than soil derived dust. It was assumed that AOT is mainly affected by mineral dust particles when $\alpha_{440\text{-}870} < 0.4$. For larger values, AOT is probably influenced by carbonaceous particles. The biomass burning activities generating these carbonaceous particles generally occur from November to March (Ogunjobi et al., 2008). Figure 3 shows that in the months February-July most of the time the $\alpha_{440\text{-}870}$ is below 0.4. It can therefore be expected that quartz grains dominate the aerosol mass in these months, which is corresponding to the main wind erosion periods in the Sahel (Sterk, 2003). Thus, AOT in the period February-July was included in further analysis (marked red in Figure 3) and AOT of October-January was excluded. The high values in July and August cannot be explained by biomass burning, because these do not take place during the rainy season. The phenomenon which caused those peaks in $\alpha_{440\text{-}870}$ remains unclear.

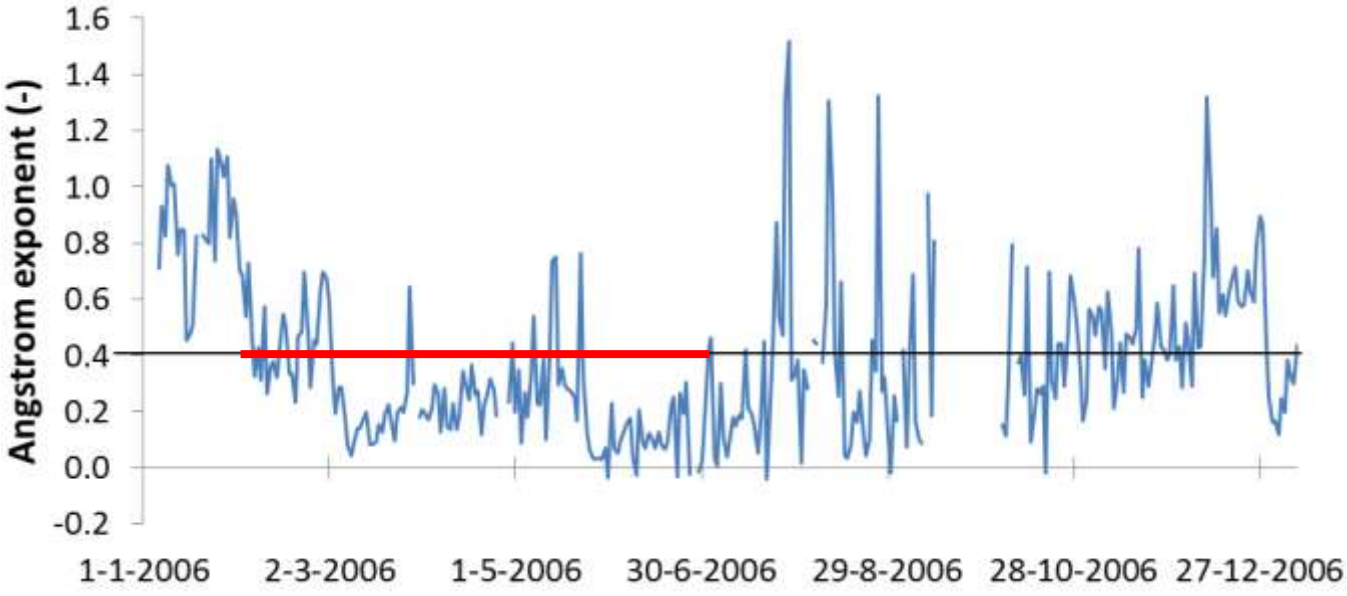

Figure 3 Daily mean Angstrom exponent for 2006 in Cinzana, Mali. All values below line α<0.4 indicate quartz grains dominated the aerosol mass. The red marked period February-July was included in further analysis of AOT.

During the rainy season from May-July the AOT signal may have been disturbed due to high concentrations of water vapour in the atmosphere. Precipitable water in the AERONET database represents the amount of water vapour in a vertical column of atmosphere. Simultaneous point measurements of AOT_{440} and precipitable water were used to investigate the suggested relation. Figure 4 shows there is no clear relation between the amount of precipitable water and AOT_{440}.

The months February-July fall within the two dust storm seasons discussed in section 2.1. For further analysis of the dry season dust storms the months February-April were taken into account and for the early rainy season the months May-July.

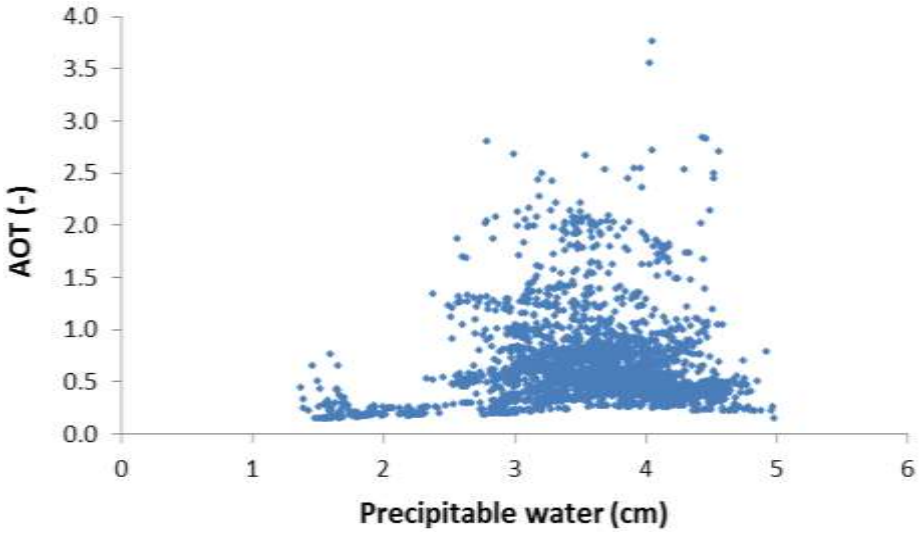

Figure 4 AOD_{440} plotted against precipitable water from May-July in Banizoumbou, Niger

3.2.2 Relation daily mean AOT and PM10 in dry season

For the dry season the daily mean AOT_{440} and PM10 data of Cinzana are plotted in Figure 5. The site in Banizoumbou showed similar results, except it had missing data in the months June and July. Figure 5 shows that there might be some correlation expected between AOT and PM10 in the dry season, because the line of the PM10 follows more or less the same pattern as the AOT. However, from mid-April onwards AOT and PM10 each start to follow a different pattern: peaks occur in the AOT which are not reflected in the PM10 measurements.

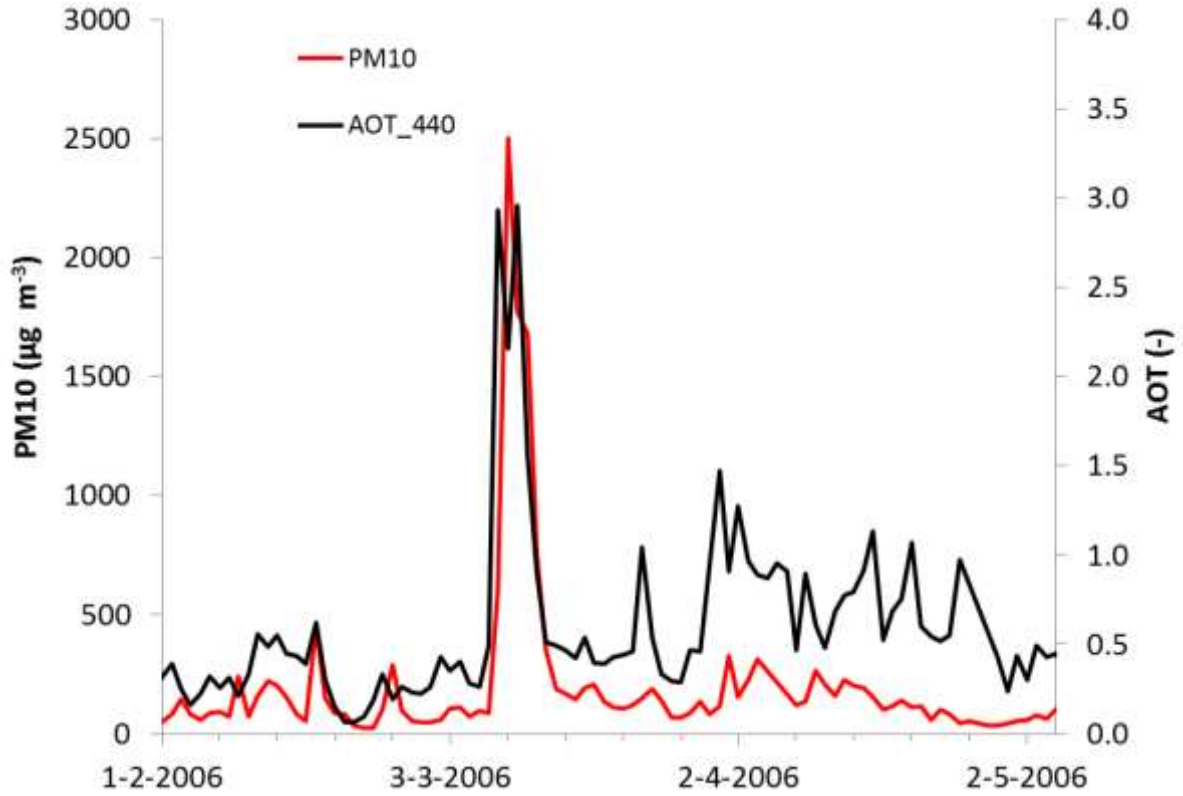

Figure 5 Daily mean PM10 and AOT for the dry season (February-April) of 2006 in Cinzana, Mali

3.2.3 *Relation daily mean AOT and PM10 in early rainy season*

For the early rainy season the daily mean AOT_{440} and PM10 data of Cinzana are plotted in Figure 6. The figure shows that the change in pattern from mid-April onward in Figure 5 continues. In the early rainy season peaks often occur in the AOT which do not appear in the dust concentration measurements. Overall, high daily mean AOT values have been observed in this season, while relatively low daily mean dust concentrations have been measured. The relatively short duration of the dust storms in the early rainy season in combination with low dust concentrations during the rest of day, may have led to generally low dust concentrations when daily means are calculated. The short duration is due to the sudden arrival of the thunderstorm and the heavy rain often followed by these dust storms which causes partial deposition of raised dust (Sterk, 2003). On the other hand, for a high correlation between dust and AOT also low daily mean values for the AOT would be expected. Manticorena et al. (2010) explain that dust originating from the Sahara and Sahelian regions can be transported at different altitudes. For example, during summer, mineral dust emitted in the Sahara is transported across the North Atlantic Ocean above the denser Marine Boundary Layer within the Saharan Air Layer (SAL). Because AOT measurements are done over the entire depth of the atmosphere they are also able to detect dust particles in high air layers like the SAL, while ground measurements with dust filters can only measure up to a few meters above ground level and are therefore not able to detect dust in high air layers.

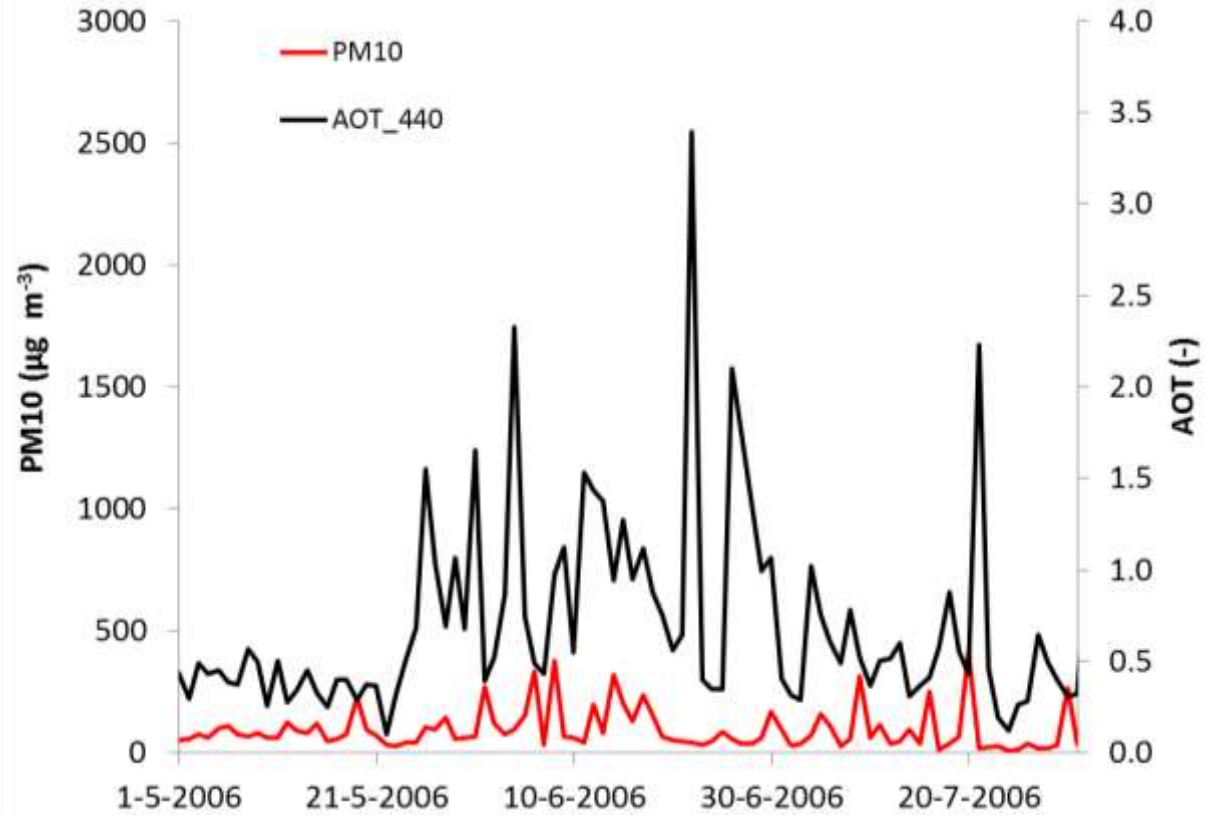

Figure 6 Daily mean PM10 and AOT for the early rainy season (May-July) of 2006 in Cinzana, Mali

For the periods where a high correlation was expected based on Figure 5 and Figure 6 and based on the Angstrom Exponents ($\alpha_{440\text{-}870}$ <0.4) a linear regression between AOT and PM10 was performed. This resulted in the implementation of the regression analysis on the months February, March and April, which are only dry season months. The results of the regression are shown in Figure 7 and the corresponding regression equations are:

$$\text{Cinzana: } PM10 = 635.64\ AOT - 140.24 \qquad (R^2 = 0.76) \qquad (3.1)$$

$$\text{Banizoumbou: } PM10 = 668.02\ AOT - 197.94 \qquad (R^2 = 0.78) \qquad (3.2)$$

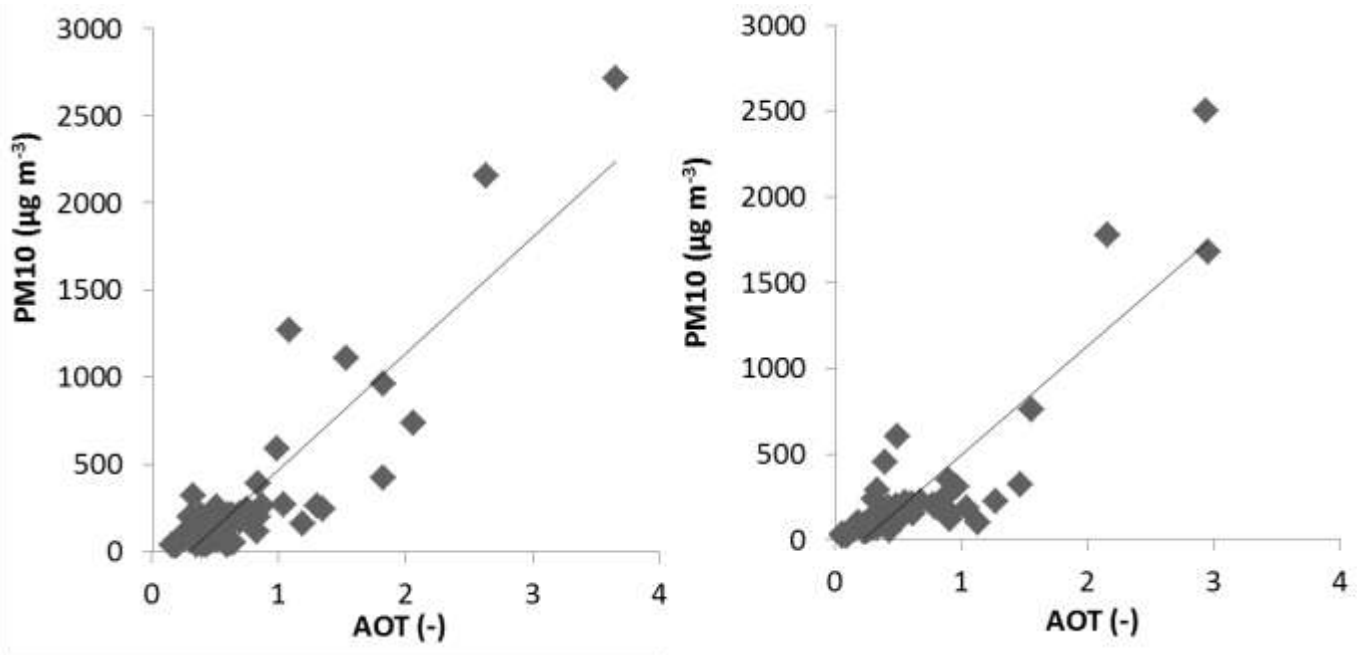

Figure 7 Linear regression of PM10 and AOT_{440} daily means from Banizoumbou (left) and Cinzana (right)

3.2.4 Relation sub-daily AOT and PM10 in early rainy season

Use of daily mean PM10 and AOT data gives poor results for the early rainy season. This may be due to the short duration of the dust storms in this season in combination with low dust concentrations during the rest of day, which leads to generally low dust concentrations when daily means are calculated. The exclusion of the early rainy season months May-July from the linear regression was attempted to be solved with PM10 data collected every 5 minutes. Because of the irregular character of the time of measurement of the AOT in the AERONET database, these 5 minute PM10 data were expected to have high potential to coincide with AOT measurements.

The time series of the 5 minute PM10 data for Cinzana are shown in Figure 8 for the dry season (Jan-April) and in Figure 9 for the early rainy season (May-July). Note the

different scales on the y-axis of Figure 8 and Figure 9. The 5 minute data for Banizoumbou showed similar results accept for missing data in June and July. Figure 9 shows that in the early rainy season the highest dust concentrations were measured. The Harmattan storms have approximately a factor ten lower dust concentrations than the storms during the early rainy season. In the dry season the largest peak in dust concentration occurred in March, which lasted for a couple of days. The high peaks in dust concentration in the early rainy season last only for a maximum of a few hours. The difference in duration and peak concentrations reflect the typical differences between the dust storms of the two seasons (Sterk, 2003).

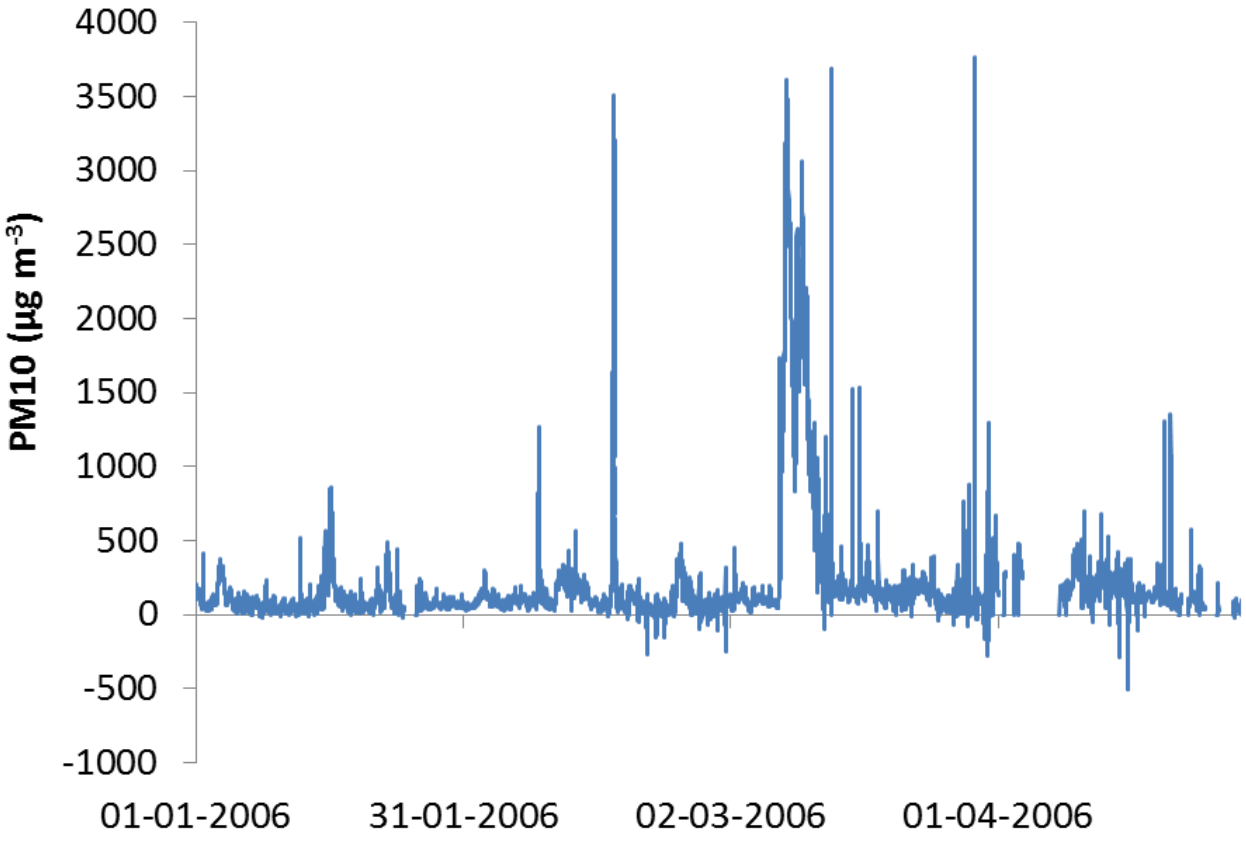

Figure 8 PM10 5min dust concentrations during dry season for Cinzana

A dataset with simultaneous 5 minute PM10 data and AOT measurements for 2006 was prepared for Banizoumbou. Unfortunately, PM10 data for June and July were missing and therefore only data for May is presented (Figure 10). Apparently, the dust concentration peaks in the 5 minute PM10 data most of the time did not coincide with the peaks in AOT. Measurements of AOT were sometimes done just before or just after a dust storm or the storm occurred during night time, when no AOT measurements were performed.

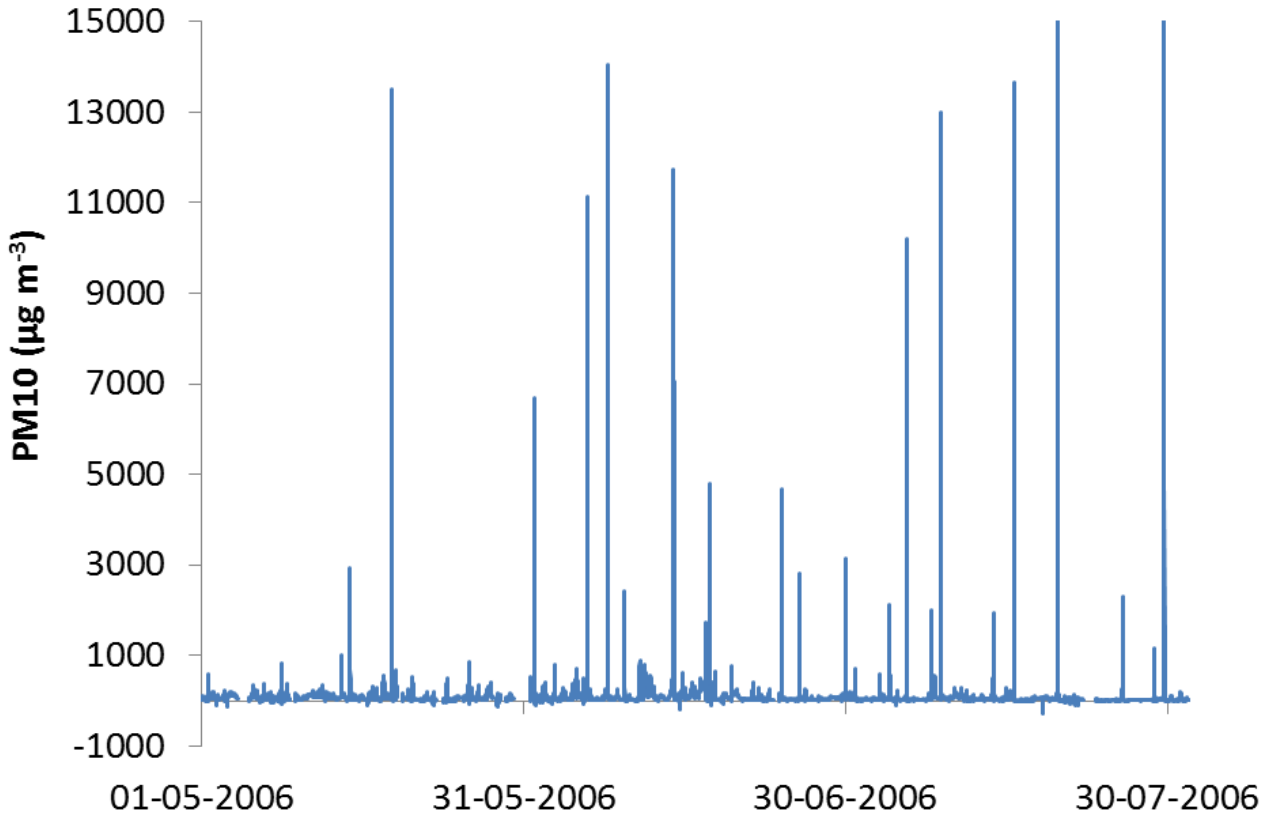

Figure 9 PM10 5min dust concentrations during early rainy season for Cinzana

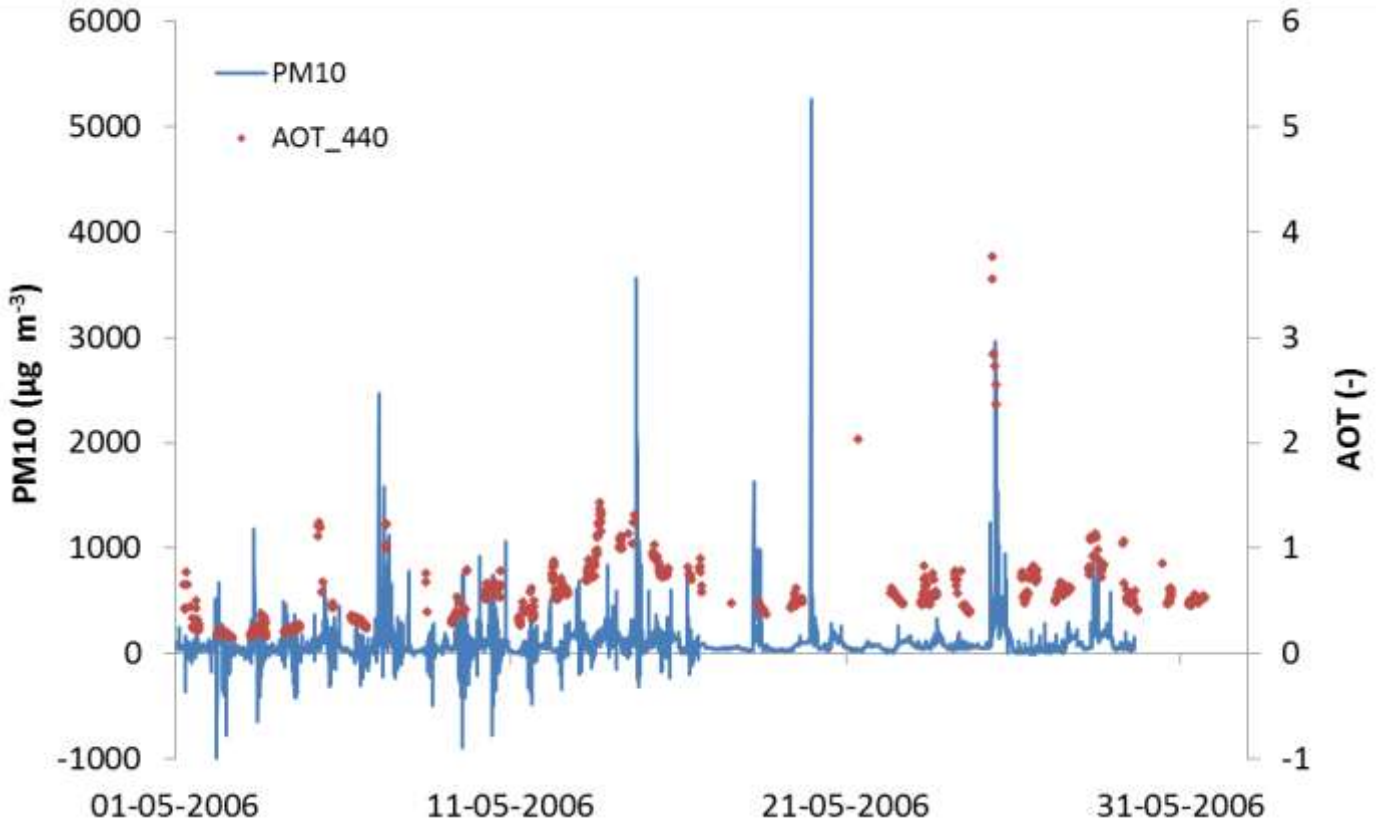

Figure 10 AOT and PM10 5 minute dust concentrations, May 2006, Banizoumbou, Niger

Nevertheless, a linear regression was performed on the sub-daily data from February-May. The results are shown in Figure 10. Measurements could only be included in the linear regression if both an AOT and PM10 observations were available. It can be observed that most high dust concentrations (PM10 > 1000 µg m^{-3}) with related high AOT values (>2) were measured in March. Only two peak dust concentrations could be included in May, because other peaks in dust concentration were not recorded in the AOT measurements. The same missing data for AOT during peak dust concentrations occurred in the 5 minute PM10 data of Cinzana in May–July. Moreover, in Figure 11 the linear regression is calculated for March and May separately. The highest correlation (R^2 =0.78) between AOT and dust concentration was found for March, similar to the relations between daily mean PM10 and AOT measurements in the dry season (equations 3.1 and 3.2). This is mainly due to the simultaneous measurements of AOT and dust concentration during peak concentrations. In February and April simultaneous measurements of high dust concentration and high AOT were scarce, therefore regression coefficients in these months are low; respectively 0.39 and 0.61. For the early rainy season dust storms in May the R^2 is 0.11. This is probably due to the fact that most high values of AOT (> 2.5) measured in May do not correspond with high dust concentrations, which causes a poorer regression for this month. As already explained, this may be due to the detected dust in the SAL with AOT measurements, while PM10 only measured up to a few meters above the ground.

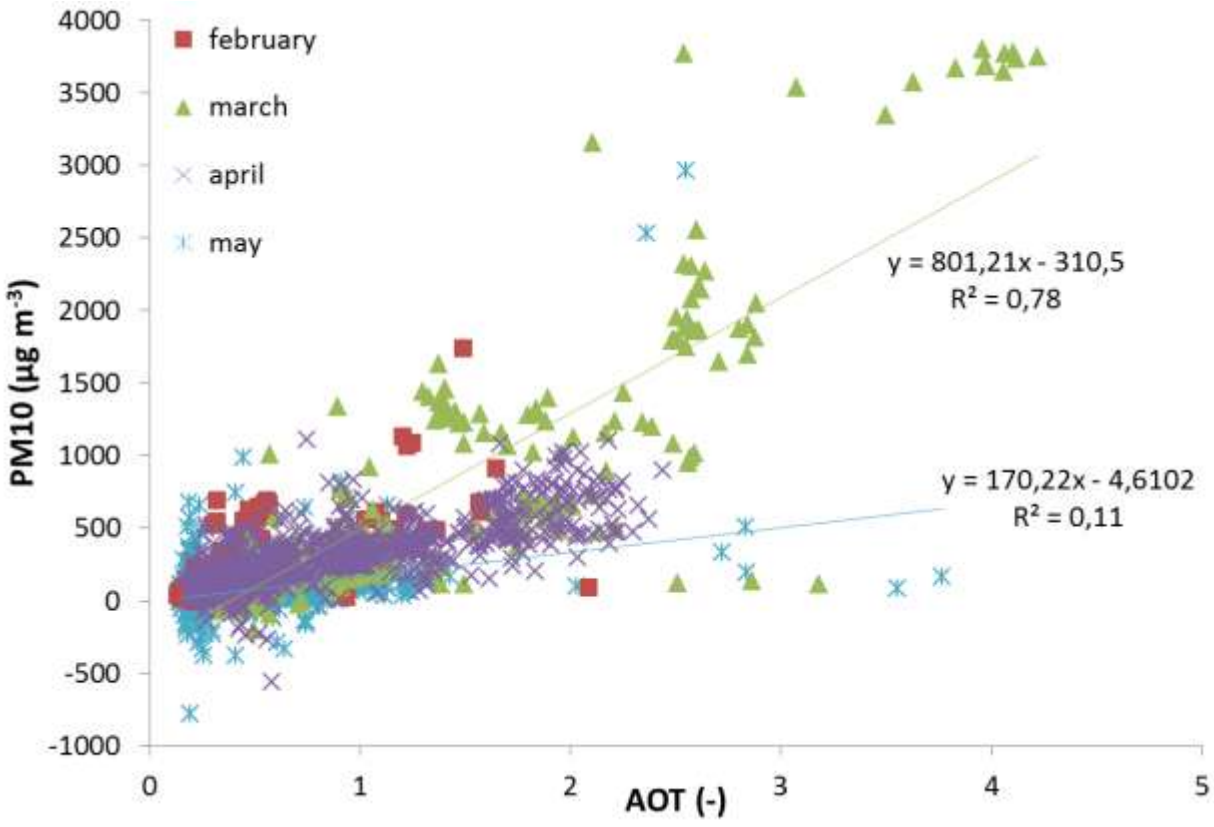

Figure 11 PM10 vs. AOT_{440} for point measurements January – May 2006 per month in Banizoumbou

3.3 Relation between AOT in-situ measurements and BT

As mentioned in section 3.1, of all dust storms observed in the RGB images only two storms could be selected in March and five storms in May, which crossed one of the ground measurement stations. For some storms a complete time series of AOT measurements was available for the whole duration of the storm and for some only a few point measurements (table 2).

Table 2 Selected dust storms from EUMETSAT MSG Dust product. In total 139 simultaneous observations of AOT and brightness temperature.

Storm date	No. available observations	Range of AOT values (-)		Range of BT_{11} (K)		Range of BT_{11-8} (K)		Range of BT_{12-11} (K)	
		min	max	min	max	min	max	min	max
18-03	2	1.31	3.20	292.99	309.73	2.97	5.64	-0.71	1.52
23-03	14	1.42	2.48	294.15	305.96	1.83	4.41	-0.80	1.11
07-05	25	0.44	0.57	297.93	319.48	4.38	6.63	-3.30	-0.28
08-05	12	0.51	2.44	288.09	319.06	0.30	6.63	-3.57	-0.14
09-05	24	1.30	1.59	300.87	316.94	3.76	5.80	-0.62	1.46
26-05	40	1.00	2.67	273.37	304.79	-1.80	3.71	-3.98	-0.54
31-05	22	0.74	3.27	267.86	303.14	-2.32	2.62	-6.43	-1.47
Overall	139	0.44	3.27	267.86	319.48	-2.32	6.63	-6.43	1.52

3.3.1 Multiple linear regression with brightness temperature and AOT

In total 139 simultaneous observations of AOT and brightness temperature could be included in the multiple linear regression (table 2). This resulted in the following regression equation ($R^2 = 0.69$):

$$\mathrm{AOT} = -7.01 + 0.032\ \mathrm{BT}_{11} - 0.354\ \mathrm{BTD}_{11-8} + 0.245\ \mathrm{BTD}_{12-11} \qquad (3.3)$$

P-values of the separate t-tests of the regression coefficients were all found to be < 0.005. Thus, it appears that all of the brightness temperature bands are of significant value to obtain the AOT from the images.

3.3.2 Principal Component Analysis of the dust storm representation with bands $BTD_{12.0-10.8}$, $BTD_{10.8-8.7}$ and $BT_{10.8}$

A Principal Component Analysis (PCA) is used to identify how much each band contributes to the RGB representation of a dust cloud, with $BTD_{12.0-10.8}$ on red, $BTD_{10.8-8.7}$ on green; and $BT_{10.8}$ on blue. From the eigenvalues of the first two principal components (Table 3) it was expected to find which bands have the largest contribution to displaying the magenta coloured dust storms. This can be found in the eigenvector values of the first two principal components. In the PC score column for each image is given how much each principal component explains of the dust storm representation with bands $BTD_{12.0-10.8}$ $BTD_{10.8-8.7}$ and $BT_{10.8}$. The PC loadings column shows how much each BT

band explains within these principal components. It is found that all three bands have a significant contribution to each RGB dust storm representation. Therefore, no simplification can be made by excluding one or two of these three variables to represent the brightness temperature for these dust storms. It is noteworthy that in March the PC loadings of $BTD_{12\text{-}11}$ in the first PC are highest and in May the $BTD_{11\text{-}8}$ and BTD_{11} are dominant in the first PC. For the second PC the contribution of $BTD_{12\text{-}11}$ also shows large differences between storm in March and May. It remains unknown what causes these effects.

Table 3 Results of principal component analysis

storm date	time	PC score			PC loadings (%)		
		PC	value	(%)	BTD12-11	BTD11-8	BT11
18-03	8:00	1	2.062	68.7	40	31	29
		2	0.633	21.1	0	45	55
		3	0.305	10.2	60	24	16
	13:00	1	2.084	69.5	59	34	7
		2	0.548	18.3	2	33	65
		3	0.369	12.3	38	34	28
08-05	7:45	1	1.885	62.8	13	41	46
		2	0.899	30.0	84	15	1
		3	0.215	7.2	4	44	52
	10:45	1	1.907	63.6	6	47	47
		2	0.943	31.4	94	4	2
		3	0.149	5.0	0	50	50
09-05	12:00	1	1.960	65.3	26	39	35
		2	0.680	22.7	69	4	27
		3	0.360	12.0	5	57	38

3.4 Relation between BT and dust concentration

3.4.1 Relation between BT and dust concentration

To obtain the relation between BT and dust concentration, the relation with AOT as proxy for the brightness temperatures (equation 3.3 with $R^2 = 0.69$) was substituted into the relations for dust concentration from AOT (equation 3.1 with $R^2 = 0.76$ and 3.2 with $R^2 = 0.78$). This resulted in the following equations for Cinzana and Banizoumbou:

$$\text{Cinzana: } PM10 = 20.34\ BT_{11} - 225.02\ BTD_{11-8} + 155.73\ BTD_{12-11} - 4596.08 \quad (3.4)$$

$$\text{Banizoumbou: } PM10 = 21.38\ BT_{11} - 236.47\ BTD_{11-8} + 163.66\ BTD_{12-11} - 4880.62 \quad (3.5)$$

The coefficients of both equations are comparable. When dust concentrations were calculated for both stations with the same values for the three brightness temperature coefficients (Table 4), they differ up to approximately 10 μg m^{-3}, while the calculated

PM10 values range between 750-900 µg m^{-3} for both stations. Thus, both equations obtained only a difference of maximum 0.15 % for the same storm.

Table 4 Comparison of outcome of equations 3.4 and 3.5. Difference is calculated as Cinzana-Banizoumbou. Brightness temperatures were taken from the 23-03-2013 dust storm observed over Zinder Airport.

BT11	BT11-8	BT12-11	Calculated PM10		Difference	
(K)	(K)	(K)	Cinzana (K)	Banizoumbou (K)	(K)	(%)
294.15	1.83	-0.80	849.54	843.56	5.97	0.7
295.55	2.01	-0.34	909.53	906.61	2.91	0.3
296.56	2.21	-0.56	850.36	844.44	5.92	0.7
297.68	2.44	-0.25	870.57	865.69	4.88	0.6
300.75	3.16	-0.12	792.56	783.73	8.84	0.11
305.96	4.41	0.75	750.20	739.24	10.96	0.15
305.96	4.41	1.11	806.82	798.75	8.08	0.10

3.4.2 Application on dust storm images of 2013

The relation found for Banizoumbou has been applied on the dust storm at 23-03-2013 in Figure 2 to investigate the range the calculated dust concentrations. The dust concentrations varied from -648.5 to 1137.1 µg m^{-3} within the dust cloud. The negative values are unrealistic, but also the maximum value is relatively low for a Harmattan dust storm, considering the measured values up to 4000 µg m^{-3} in 2006 (Figure 8). However, if this dust storm may already have been in a dissipating phase at 12:00 a maximum concentration of 1137.1 µg m^{-3} is still acceptable.

Even though the empirical relations are limited in its application outside the dry season, is has been tested on one of the dust storms detected in the early rainy season. The selected storm occurred on 24-06-2013 at the border of Niger and Mali (Figure 12), moving from south-east to north-west. Its dust concentration per pixel was calculated from the image at 04:00 AM with the relation obtained for Banizoumbou (equation 3.5). Dust concentrations in the dust storm cloud varied from 800-1300 µg m^{-3}. It must be noted that validation of the result was not possible, due to lack of dust concentration ground data. Although the calculated dust concentrations are realistic values for a dust storm in general, they are approximately a factor 10 lower if compared with the measured PM10 values in 2006 (Figure 9). This may be explained by the fact that such high dust concentrations have not been measured in the months February-April on which equation 3.5 is based. Extrapolation towards early rainy season dust storm is clearly not applicable.

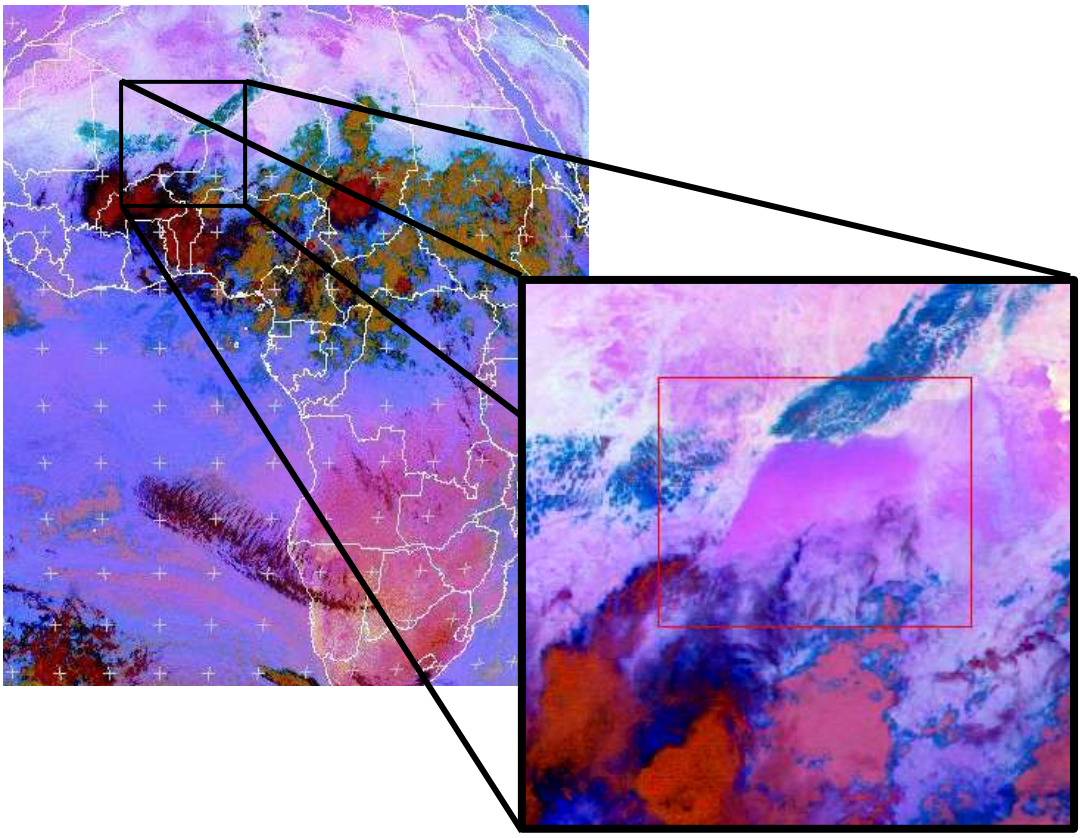

Figure 12 RGB Dust image of dust storm on 24-06-2013 at 04:00 at the border of Niger and Mali. Again the overview image is taken from the EUMETSAT MSG Dust product by Benincasa (2012). Zoom window is the RGB composite in ENVI used for dust calculation. For both frames R: $IR_{12.0}$- $IR_{10.8}$, G: $IR_{10.8}$-$IR_{8.7,}$ B: IR_{10}.

4. Discussion and conclusions

4.1 Ground data

The relation between AOT and dust concentration measured at observations stations at ground level was determined for two important dust storm seasons. A good relation was obtained for Harmattan dust storms ($R^2 > 0.75$), because of high dust concentrations lasting for multiple days. Due to the relatively constant dust concentration the correlation between AOT and PM10 for the daily mean and 5 minute data hardly differed. The obtained correlation coefficients are higher than those found by Deroubaix et al. (2013), which were 0.27-0.40. They investigated the capability of the aerosol index (AI) derived from the ozone monitoring instrument (OMI) to represent PM10. However, the relation between AOT and PM10 found in this study holds only for the period where AOT is not disturbed by carbonaceous particles due to biomass burning. In 2006 this only applied to February, March and April in the Harmattan season and May-July in the early rainy season. These selected periods are confirmed by Rajot et al. (2008). They found, also based on Angstrom exponent measurements, that the coarse mineral dust dominated the overall aerosol in the Sahel during February–July in 2002-2007.

Atmospheric water was also expected to disturb the AOT measurements, especially during the rainy season. However, this was probably not the case since no relation between precipitable water and AOT_{440} was found. This is in accordance with Holden et al. (2001), who reported that AOT_{500} and precipitable water (cm) showed no significant correlation at the Mauna Lea Observatory on Mauna Lea, Hawaii. On the other hand, Myhre et al. (2007) found an increase in cloud cover, used a proxy for atmospheric water, with AOT even in regions with relatively hydrophobic aerosols, such as dust aerosols. However, their analysis was partly based on MODIS satellite data and they noted it cannot be ruled out that MODIS interpreted dust as clouds.

A poor relation between AOT and dust concentration was obtained for the early rainy season storms ($R^2 = 0.11$), mainly due to gaps in the AOT measurements. These measurements were only performed during daytime, while many of the dust storms in this season occur during the night (J.L. Rajot, personal correspondence, 2013). In addition, the measurements were done at irregular time steps due to the dependence on the position of the sun in the sky and they were not adapted to detection of dust emitted by convection. The dust events are too short in duration and peak concentrations are often missed. Even if measurements are done during such a storm, data are often rejected because AOT is too variable and too high and is often considered as a cloud (J.L. Rajot, personal correspondence, 2013).

Shortcomings in the PM10 data are in the first place the occurrence of negative values, which are unrealistic. They may occur due to water absorbed on the dust when the filter becomes overloaded during the rainy season (J.L. Rajot, personal

correspondence, 2013). These values are averaged out when mean values are calculated over a longer period (15 min, 1 hour or daily). Since the empirical relations in this study are based on daily mean PM10 values, the calculated dust concentrations will hardly be influenced by these negative values. However, it may be more realistic to consider that for these measurements dust concentrations are close to zero. Actual missing data occur when the filters are changed, but it is endeavoured to avoid changing filters during dust events.

Regrettably, no data on dust concentration for 2013 in the Sahel were available for this study. If this would have been the case, real-time coupling of satellite detected dust and in-situ measured dust could have been performed, possibly resulting in a better relation between brightness temperatures and dust concentration.

4.2 Identify dust storms

Dust storms recorded by at least one AERONET observation station were identified on the available MSG images from 2013. This was performed with the RGB Dust product band combination, with $BTD_{12.0\text{-}10.8}$ on red, $BTD_{10.8\text{-}8.7}$ on green and $BT_{10.8}$ on blue. Dust storms can be recognized by their magenta to purple colour. Since TIR gives the temperature of objects on or above the land surface it can be used to separate cool dust/water/ice clouds from the warmer land surface. The advantage of the TIR channels for dust storm detection is that they also provide information during night-time (Hao et al., 2007; Wald et al., 1998), because it is radiation emitted by the earth itself and not reflected solar radiation. However, during night-time the temperature of the earth surface drops and the differences between objects become less pronounced. In addition, the earth surface is constantly adapting its temperature due to change in received solar radiation, which is varying over the day and over the seasons. This external factor influencing the TIR channels leads to a change in the appearance of dust storms over the day in the RGB band combination with $BTD_{12.0\text{-}10.8}$ on red, $BTD_{10.8\text{-}8.7}$ on green and $BT_{10.8}$ on blue. This results in a change from a magenta to a purple colour of the same storm. It makes automatic but also manual identification of the dust storms difficult. In addition, other objects like high mountainous areas may appear in the same colours as dust storms, but dust storms can be separated from these objects by their moving, dynamic character (Meteorological Education, 2013)

Moreover, the use of the single bands $IR_{12.0}$, $IR_{10.8}$ and $IR_{8.7}$ bands (K) is not ideal for the detection of the dust storms, because it is very time consuming to calculate the $BTD_{12.0\text{-}10.8}$, $BTD_{10.8\text{-}8.7}$ and $BT_{10.8}$ bands manually for every 15 min time frame. It would be easier and faster and less sensitive to errors if the EUMETSAT RGB Dust product is directly available for analysis. For the identification phase it would have been too time-consuming to create an RGB image for every 15 min for 6 months, therefore the online animation by Benincasa (2012) was used. However, this is a compressed version (.gif) of the original images, thus spatial and spectral information is lost, which is the reason why

the raw data images were still required. In addition, the temporal resolution was reduced to 1 hour instead of 15 min, which will have resulted in non-detectability of storms with a lifetime of less than 1 hour.

4.3 Brightness temperature and AOT

To explore the relation between TIR temperature measured at the top of the atmosphere and dust concentration, AOT was used as a proxy for dust concentration, because no dust data from 2013 were available. Equation 2.3, which was derived from the multi linear regression analysis, was reasonably accurate (R^2 = 0.69). It confirms that the use of AOT as proxy for dust concentration is not optimal and it would have been be better to use images and in-situ dust concentrations of the same period.

The analysis of the separate brightness temperature and brightness temperature difference coefficients in equation 3.3 and principal component analysis confirm that all three are of significant importance to calculate AOT and therefore dust concentration (equation 3.4 and 3.5). Thus, this study, but also Li et al. (2007) and Zhang et al. (2006) correctly selected all three of these bands for analysis.

An important shortcoming of the imagery data for the detection and quantification of storms during the rainy season is the presence of large thunderclouds which block the signal of the dust storm below the cloud. Even though the dust storms are present as a 'wall' in front of the storm the cloud often covers the dust storms due to its anvil shape covering an area of tens to hundreds of kilometres at the top part. The only radiation which passes through clouds is microwave radiation (1mm-1m wavelengths), but unfortunately this also passes through atmospheric dust and can therefore not be used for dust storm detection. Additionally, as mentioned in section 4.2, the format (.hrit) in which the data is delivered results in an extra step in obtaining the images of the dust storms (appendix I). On the other hand, an advantage of this extra step is that there is more control on the type (digital numbers/radiance/temperature), spatial size and included channels of the generated images. In addition, the raw image digital numbers can be immediately transformed into reflectance/temperature values (appendix I).

The geostationary position of the satellite is a great advantage for detecting dust storms lasting less than two days, which is a common return time for polar orbiting satellites. The geostationary position becomes problematic for areas further away from the equator due to imbalance between pixel shape and actual ground surface represented by the pixel. Due to the curvature of the earth the ground area that every sensed pixel represents varies. Below the sensor (nadir) the pixel size is optimal, but it increases exponentially when moving to off nadir positions (Kraaijenbrink, 2012). Thus, close to the equator, which is the case for the Sahel, this effect is relatively small and was therefore neglected in this study.

4.4 Dust concentration and brightness temperature

To directly derive lateral dust concentrations from the SEVIRI-MSG imagery empirical equations 3.4 and 3.5 were developed for respectively Cinzana and Banizoumbou. For those equations values of $BTD_{12.0\text{-}10.8}$, $BTD_{10.8\text{-}8.7}$ and $BT_{10.8}$ obtained from a SEVIRI-MSG image can be used to calculate PM10. However, there are restrictions to the application of this empirical relation. Firstly, it is only applicable to the months February and March of the Harmattan season due to the interference of carbonaceous particles in the AOT signal from November-January. It is unclear what the influence of carbonaceous particles is in the final empirical relation, because role of AOT is not directly included anymore. If the relation is directly determined from satellite images and PM10 measurements of the same time period, it may hold for the entire Harmattan period including November-January. Secondly, the relation did not work for the early rainy season storms. As explained, this is mainly due to missing data in the AOT measurements. Thirdly, the relation holds only for the region from which data was abstracted and is therefore restricted in terms of spatial generalisation. This is confirmed by the outcome of the application of equation 3.5 on the 24-06-2013 dust storm (see section 3.4.2). This is not expected to be improved easily due to the scarce amount of ground stations measuring dust concentration. It may already be difficult to make reliable calculations for the part of the Sahel further east of Banizoumbou, due to local different composition of the dust or off nadir effects in the images. Therefore, it seems still questionable to make one single equation for the whole Sahel.

On the other hand, the western part of the Sahel (west of Banizoumbou) seems to be represented quite well by either equation 4 or 5, since they lead to quite similar results differing up to 10 μg m^{-3} for similar input values. However, the application of equation 3.5 on a nearby dust storm during the Harmattan season resulted in unrealistic dust concentrations, which could not be validated with currently available ground data. The BTs of the dust cloud probably have been outside the range of BTs on which the equation was based, leading to low, even negative, dust concentrations.

Ultimately, most wind erosion problems occur during the early rain season, when wind erosion takes place due to the presence of large thunderstorms. Unfortunately, these dust storms are often not detectable on the SEVIRI-MSG because their signal is blocked by the cloud of the thunderstorms above it. It can already be seen from the ground data that in this period extremely high dust concentrations are measured. Therefore, quantification of annual wind erosion with satellite images without inclusion of these events will lead to significant underestimation. However, the developed method may already be used to get a first estimate for eroded and deposited dust quantities in the Harmattan season.

Acknowledgements

I am grateful to Jean Louis Rajot and Beatrice Manticorena (LISA) for making the PM10 data of Banizoumbou and Cinzana available and helping with the interpretation. Didier Tanri, Bernadette Chatenet and Jean Louis Rajot are thanked for making the AOT data available from the AERONET sites. I additionally like to thank my supervisors Geert Sterk, Steven de Jong and Maarten Zeylmans Van Emmichoven for their suggestions, feedback and instruction. Finally, Philip Kraaijenbrink is gratefully acknowledged for helping with the abstraction of the images from GEONETCast.

References

Akhlaq, M., Sheltami, T. R., & Mouftah, H. T. (2012). A review of techniques and technologies for sand and dust storm detection. Reviews in Environmental Science and Bio/Technology, 11(3), 305-322.

AERONET (2013) AERONET Mission. http://aeronet.gsfc.nasa.gov/. Accessed June 2013

AMMA (2013a) AMMA International. http://amma-international.org/about/index. Accessed June 2013

AMMA (2013b) AMMA International. http://database.amma-international.org/interface.jsf. Accessed June 2013

Bai ZG, Dent DL, Olsson L and Schaepman ME 2008. Global assessment of land degradation and improvement. 1. Identification by remote sensing. Report 2008/01, ISRIC – World Soil Information, Wageningen

Benincasa, F. (2012) Dust observations by MSG – EUMETSAT. WMO Sand and dust storm warning advisory and assessment system. http://sds-was.aemet.es/forecast-products/dust-observations/msg-2013-eumetsat. Accessed August 2013

Deroubaix, A., Martiny, N., Chiapello, I., & Marticoréna, B. (2013). Suitability of OMI aerosol index to reflect mineral dust surface conditions: Preliminary application for studying the link with meningitis epidemics in the Sahel. Remote Sensing of Environment, 133, 116-127.

Dregne, H. E., & Chou, N. T. (1992). Global desertification dimensions and costs. Degradation and restoration of arid lands, 73-92.

Eswaran, H., Lal, R., & Reich, P. F. (2001). Land degradation: an overview. Responses to Land degradation, 20-35.

EUMETSAT (2004) EUMETSAT—satellites—instruments. http://www.eumetsat.int/Home/Main/Satellites/MeteosatSecondGeneration/Instruments/index.htm?l=en. Accessed June 2013

EUMETSAT (2007). GEONETCast Global Design Document, No. EUM/OPS/DOC/06/1799).

EUMETSAT (2010) EUMETSAT - overview http://www.eumetsat.int/Home/Main/AboutEUMETSAT/WhoWeAre/SP_1222084861476?l=en. Accessed June 2013

EUMETSAT (2013). GEONETCast Data Access . http://www.eumetsat.int/Home/Main/DataAccess/EUMETCast/SP_20100519114624675?l=en. Accessed June 2013

Field, J. P., Breshears, D. D., Whicker, J. J., & Zou, C. B. (2012). Sediment capture by vegetation patches: Implications for desertification and increased resource redistribution. Journal of Geophysical Research: Biogeosciences (2005–2012), 117(G1).

Geist, H. (2005) The Causes and Progression of Desertification. Burlington, Vermont, Ashgate Publishing.

Hao, X., & Qu, J. J. (2007). Saharan dust storm detection using moderate resolution imaging spectroradiometer thermal infrared bands. Journal of Applied Remote Sensing, 1(1), 013510-013510. Hinds, William C. (1999). Aerosol Technology (2nd ed.). Wiley – Interscience

Holben, B. N., Eck, T. F., Slutsker, I., Tanre, D., Buis, J. P., Setzer, A., & Smirnov, A. (1998). AERONET—A federated instrument network and data archive for aerosol characterization. Remote sensing of environment, 66(1), 1-16.

Holben, B. N., Tanre, D., Smirnov, A., Eck, T. F., Slutsker, I., Abuhassan, N., & Zibordi, G. (2001). An emerging ground-based aerosol climatology: Aerosol optical depth from AERONET. Journal of Geophysical Research: Atmospheres (1984–2012), 106(D11), 12067-12097.

Jones, A., Breuning-Madsen, H., Brossard, M., Dampha, A., Deckers, J., Dewitte, O. and Zougmoré, R. (2013). Soil atlas of Africa.

Knippertz, P., & Todd, M. C. (2012). Mineral dust aerosols over the Sahara: Meteorological controls on emission and transport and implications for modeling. Reviews of Geophysics, 50(1)

Kraaijenbrink, P. (2012) Processing of GEONETCast Data for Use in Physical Geographic Research. A Guided Research Report, Utrecht University

Lantieri, D., (2006) Potential Use of Satellite Remote Sensing for Land Degradation Assessment in Drylands. Application to the LADA Project. FAO Environment and Natural Resources Service.

Lemmens, R., Maathuis, B. H. P., Mannaerts, C. M., Foerster, T., Schaeffer, B., Wytzisk, A. (2009): Web-based spatial analysis with the ILWIS open source GIS software and satellite images from GEONETCast. Presentation at AGU Fall Meeting, Dec 14 – 18, 2009. San Francisco, USA.

Lensky, I. M., & Rosenfeld, D. (2008). Clouds-aerosols-precipitation satellite analysis tool (CAPSAT). Atmospheric Chemistry and Physics, 8(22), 6739-6753.

Li, J., Zhang, P., Schmit, T. J., Schmetz, J., & Menzel, W. P. (2007). Technical note: Quantitative monitoring of a Saharan dust event with SEVIRI on Meteosat-8. International journal of remote sensing, 28(10), 2181-2186

Li, S. U. N., Xiang-Ao, X. I. A., Pu-Cai, W. A. N. G., Hong-Bin, C., GOLOUB, P., & Wen-Xing, Z. H. A. N. G. (2013). Identification of Aerosol Types and Their Optical Properties in the North China Plain Based on Long-Term AERONET Data. Atmospheric and Oceanic Science Letters, 3.

Marticorena, B., Chatenet, B., Rajot, J. L., Traoré, S., Coulibaly, M., Diallo, A., ... & Zakou, A. (2010). Temporal variability of mineral dust concentrations over West Africa: analyses of a pluriannual monitoring from the AMMA Sahelian Dust Transect. Atmospheric Chemistry and Physics, 10(18), 8899-8915.

Meteorological Education (2013) Training Module: Forcasting Dust Storms. https://www.meted.ucar.edu Accessed July 2013

Myhre, G., Stordal, F., Johnsrud, M., Kaufman, Y. J., Rosenfeld, D., Storelvmo, T., and Isaksen, I. S. A. (2007). Aerosol-cloud interaction inferred from MODIS satellite data and global aerosol models. Atmospheric Chemistry and Physics, 7(12), 3081-3101.

Oldeman, L.R. (1994) Global Extend of Soil Degradation. In: Greenland, D.J., Szabolcs, I. (1994) Soil Resilience and Sustainable Land Use. Wellingford, UK

Ogunjobi, K. O., He, Z., & Simmer, C. (2008). Spectral aerosol optical properties from AERONET Sun-photometric measurements over West Africa. Atmospheric Research, 88(2), 89-107.

Rajot, J. L., Formenti, P., Alfaro, S., Desboeufs, K., Chevaillier, S., Chatenet, B., Gaudichet, A., Journet, E., Marticorena,B., Triquet,S., Maman, A.,Mouget, N., Zakou, A. (2008). AMMA dust experiment: An overview of measurements performed during the dry season special observation period (SOP0) at the Banizoumbou (Niger) supersite. Journal of Geophysical Research: Atmospheres (1984–2012), 113(D23).

Schepanski, K., Tegen, I., & Macke, A. (2012). Comparison of satellite based observations of Saharan dust source areas. Remote Sensing of Environment, 123, 90-97

Schmid, B., Michalsky, J. J., Slater, D. W., Barnard, J. C., Halthore, R. N., Liljegren, J. C., ... & Slutsker, I. (2001). Comparison of columnar water-vapor measurements from solar transmittance methods. Applied Optics, 40(12), 1886-1896.

Shao, Y. (2008). Physics and modelling of wind erosion. Springer.

Sterk, G. (2003). Causes, consequences and control of wind erosion in Sahelian Africa: a review. Land Degradation & Development, 14(1), 95-108.

Sterk, G., & Goossens, D. (2007). Emissions of soil dust and related problems in Europe: an overview. In Proceeding on Dust Conference (pp. 23-24).

Symeonakis, E., & Drake, N. (2004). Monitoring desertification and land degradation over sub-Saharan Africa. International Journal of Remote Sensing, 25(3), 573-592.

Tetzlaff, G., & Peters, M. (1986). Deep-sea sediments in the eastern equatorial Atlantic off the African coast and meteorological flow patterns over the Sahel. Geologische Rundschau, 75(1), 71-79.

UNCCD (2011) Desertification – a visual synthesis. Bonn, Germany

UNEP (1997) World Atlas of Desertification. Second Edition. Nairobi, UNEP

Vogt, J. V., Safriel, U., Von Maltitz, G., Sokona, Y., Zougmore, R., Bastin, G., & Hill, J. (2011). Monitoring and assessment of land degradation and desertification: towards new conceptual and integrated approaches. Land Degradation & Development, 22(2), 150-165.

Wald, A. E., Kaufman, Y. J., Tanré, D., & Gao, B. C. (1998). Daytime and nighttime detection of mineral dust over desert using infrared spectral contrast. Journal of Geophysical Research: Atmospheres (1984–2012), 103(D24), 32307-32313.

Wessels, K.J. (2009) Comments on 'Proxy global assessment of land degradation' by Bai et al. (2008). Soil Use and Management 25: 91–92.

WMO (2010) Guide to Agricultural Meteorological Practices (GAMP) 2010 Edition (WMO-No. 134)

Xu, D., Qu, J. J., Niu, S., & Hao, X. (2011). Sand and dust storm detection over desert regions in China with MODIS measurements. International Journal of Remote Sensing, 32(24), 9365-9373

Zhang, P., Lu, N., Hu, X., Dong, C. (2006) Identification and physical retrieval of dust storm using three MODIS thermal IR channels. Global and Planetary Change 52, 197–206

Appendices

Appendix I – MSG Data Retriever

The MSG Data Retriever interface is shown in figure A1. The different settings for this study are discussed in this appendix. From the 'Satellite' drop down list the MSG2 satellite was specified at all times. These settings refer to the regular MSG 9 situated at 0 degree (scanning the whole field of view of MSG at 15 minutes temporal intervals). For the 'Date / Time range' settings the preselect time frame during the pre-processing phase (section 2.3.2) is filled in. The repeat interval was set at the minimum of 15 minutes. Since time series were produced the box Multiple Times in one File was checked for 'Series' and per MSG channel such a time series was produced. Conversion of original digital values to Temperature was selected for 'Conversion' in order to obtain direct TIR temperatures.

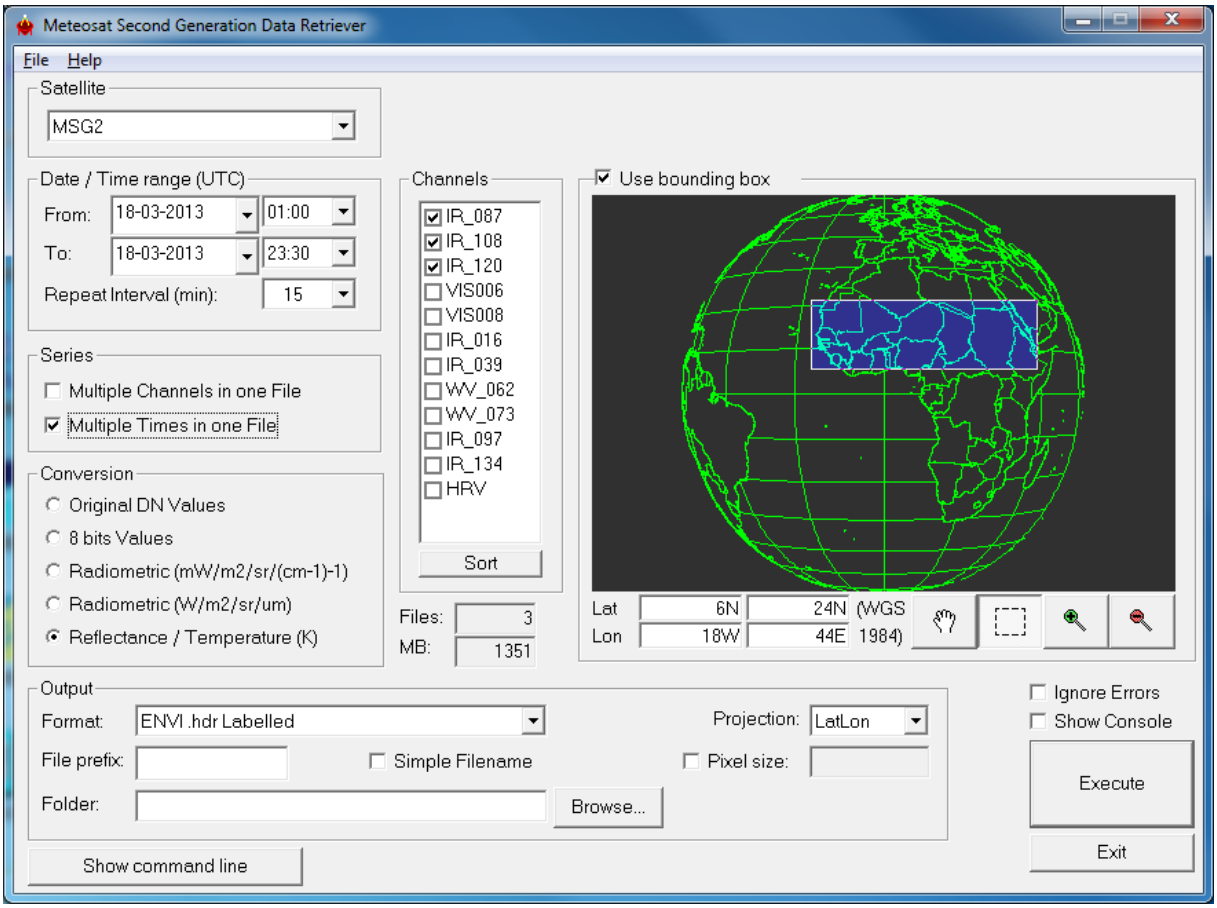

Figure A1 MSG Data Retriever interface

For the 'Channels' IR_120, IR_108 and IR_087 were selected, needed to calculate $BTD_{12.0\text{-}10.8}$, $BTD_{10.8\text{-}8.7}$ and $BT_{10.8}$ in a later stage with the ENVI software using Band Math. The bounding box was set al Lat 6N; 24N and Lon 18W; 44E.

Settings for the output were ENVI format file and a Lat/Lon projection to get the right georeferencing for the image.

Appendix II – Principal Component Analysis in ENVI

This appendix gives the stepwise obtaining of the contribution of the brightness temperature bands to the principal components of a dust storm image.

1. Open ENVI
2. Open the RGB Dust image with layers $BTD_{12.0-10.8}$, $BTD_{10.8-8.7}$ and $BT_{10.8}$.
3. Perform principal component analysis: Transform > Principal Component > Forward PC rotation > Compute new statistics
4. Check "Correlation Matrix" instead of "Covariance Matrix" , because there is a large difference in Kelvin between BTD and BT.
5. Save the forward rotated file and the statistics file (.sta)
6. Save the given eigenvalues from the ENVI plot to a .txt file; these represent the PC score.
7. Open the statistics file: Basic tools > Statistics
8. In the new window: File > Save current covariance to image. A new file as [Memory] with Covariance, Correlation and Eigenvector as layers appears.
9. Calculate the contribution of the bands with: Basic Tools > Band Math and fill in: (b1^2)*100 with b1 linked to the Eigenvector layer of [Memory]
10. Load the obtained [Band Math] band
11. Abstract the contribution of the bands per PC with:
    Tools > Profiles > X Profile.
    The profile of the top row shows the contribution on the y-axis (%) and bands on the x-axis for the first PC.
    The second row for the second PC and the third row for the third PC.